Stress-induced TFIIIC binding to Alu elements controls gene expression via chromatin looping and histone acetylation

Roberto Ferrari[*1§], Lara Isabel de Llobet Cucalon[*1], Chiara Di Vona[1], François Le Dilly[1], Enrique Vidal[1], Antonios Lioutas[1], Javier Quilez Oliete[1], Laura Jochem[3], Erin Cutts[3], Giorgio Dieci[2], Alessandro Vannini[3], Martin Teichmann[4], Susana de la Luna[1,5,6] and Miguel Beato[1,5,§]

Affiliations

1- Gene Regulation Stem Cells and Cancer Program, Center for Genomic Regulation (CRG), Barcelona Institute of Science and Technology (BIST), Barcelona, Spain

2- Department of Chemistry, Life Sciences and Environmental Sustainability, University of Parma, Parco Area delle Scienze 23/A, Parma, Italy

3- The Institute of Cancer Research (ICR). London, SW3 3RP. UK.

4- Université de Bordeaux INSERM U1212 - CNRS UMR 5320 146, rue Léo Saignat 33076 Bordeaux France

5- Universitat Pompeu Fabra (UPF), Barcelona, Spain

6- Institució Catalana de Recerca i Estudis Avançats (ICREA), Barcelona, Spain

* These authors contributed equally to this work.

§ Co-corresponding authors: roberto.ferrari@crg.eu, miguel.beato@crg.eu

Abstract

The mammalian genome is shaped by the expansion of repetitive elements and its folding is governed by epigenetic modifications and architectural proteins. However, the precise way all these factors interact to coordinate genome structure and expression is poorly understood. Here we report that upon serum starvation TFIIIC, a general transcription factor, binds a subset of Alu elements close to cell cycle genes and rewires genome topology via direct histone acetylation and promoter-anchored chromatin loops to distant genes. These changes ensure basal transcription of crucial cell cycle genes and their re-activation upon serum re-exposure. Our study unveils a novel function of TFIIIC on gene expression and genome folding achieved through casting direct manipulation of the epigenetic state of Alu elements to adjust 3D genome function.

Keywords

TFIIIC, Alu elements, repetitive elements, H3K18ac, histone acetylation, breast cancer, CTCF, Hi-C, 3D genome structure, Pol II, Pol III, cell cycle, ADPN, serum starvation

Transcriptional regulation is crucial for the organization and coordination of cellular functions during rapid changes in environmental conditions (*1*). In the last decade, it has become clear that 3D folding of the eukaryotic genome is an important regulatory element in transcriptional control (*2*). Changes in genome organization result from the combined action of specific transcription factors (TFs), architectural proteins, such as CCCTC-binding factor (CTCF) and Cohesins, together with DNA/chromatin elements (*2*). In this context, the expansion of several families of transposable elements (TE) has provided new regulatory network for coordinated control of gene expression (*3*) and enabled more sophisticated avenues for genome organization (*4, 5*). Short Interspersed Elements (SINEs), in particular Alu elements (AEs), represent the largest fraction of TE which have also evolved proto-enhancers function in the human genome (*6*). AEs are transcribed by RNA polymerase (Pol) III, a nutrient-sensing machinery (*7*) that is recruited to chromatin by TFIIIC and TFIIIB and also transcribes tRNA and other small non-coding RNA genes (*8*). Besides its known function in Pol III transcription, TFIIIC plays other roles in the nucleus, in particular as an architectural protein of the yeast genome (*9*). However, how TFIIIC participates in 3D organization of the mammalian genome remains elusive. We explore this question in the context of serum starvation (SS), a method widely used to synchronize cultured cells (*10*). Noteworthy, overcoming SS and reduced nutrient availability is an essential process for the survival of malignant cells in solid tumors (*11*).

Given the importance of Pol III in the response to stress (*12*), we assessed the genome occupancy of TFIIIC in T47D breast cancer cells growing in normal condition (+S) and after 16

h of SS (-S) (fig. S1A), which did not alter significantly the cell cycle profile (fig. S1B, χ^2 test = 0.09). Surprisingly, SS induced a large number of new TFIIIC binding sites, passing from 388 to 3262 (Fig. 1A), but did not change occupancy by another insulator protein, CTCF (Fig. 1B). In normal growth conditions only ~30% (140) of the total TFIIIC peaks were located over AEs, while after SS this value increased to 89% (3096) (Fig. 1, C and D). Word cloud analysis of major repetitive elements (RE) bound by TFIIIC upon SS showed AEs as highly enriched, in particular the AluSx family (fig. S1C), a ~30 million years old Alu lineage (*13*). AEs bound by TFIIIC are *bona fide* functional AEs as defined by having intact A- and B-boxes, and the B-box consensus of extra-TFIIIC sites (ETC) sites (*14*) was only found for 459 occupied sites (14% of the SINEs bound by TFIIIC under SS) (fig. S1D).

A very large fraction of new TFIIIC binding sites were found in close proximity (within 5 kb) of annotated Pol II transcription start sites (TSS) (Fig. 1, D and E), enriched for cell cycle-related functions (fig. S1E). We named these sites TAPs (TFIIIC-associated Pol II promoters) (Fig. 1E). In contrast to the tRNA genes, other components of the Pol III machinery were not enriched at the TFIIIC-bound AEs (Fig. S1F). Notably, the TFIIIC enrichment at AEs close to TAPs was not simply reflecting a higher AE density, since AE's density was higher at Pol II TSS devoided of TFIIIC than at TAPs (Fig. S1G).

Increased AEs occupancy by TFIIIC was also observed in other normal and cancer cell lines subjected to SS, such as the glioblastoma cell line T98G, the normal lung fibroblasts IMR90 and normal breast MCF10A cells (fig. S2A), which also exhibited the increase in TAPs (Fig. 1F and S2B). Occupancy of AEs by TFIIIC in T47D cells was reversed after just 30 min of serum re-

addiction, indicating a rapidly reversible process and ruling out a cell-cycle direct role (Fig. 1G and S2C). Thus, in response to SS TFIIIC is reversibly recruited to AEs close to the Pol II promoters of a subset of cell cycle-related genes.

To explore how TFIIIC is selectively recruited to the TAPs we affinity-purified chromatin-associated TFIIIC with an antibody against the second largest subunit (GTF3C2), followed by identification of the associated proteins by mass spectrometry. All six subunits of TFIIIC were identified as positive interactors (Fig. 2A, Table S1), validating the approach. Interestingly, all subunits of the recently characterized ChAHP complex (*15*) were also identified, with two of which, the chromodomain helicase DNA binding protein 4 (CHD4) and the activity-dependent neuroprotector homeobox (ADNP), appearing as top TFIIIC interactors (Fig. 2A, Table S1). Furthermore, we demonstrated that human ADNP directly interacts with TFIIIC in vitro, using recombinant complexes produced in insect cells (fig. S3A). ADNP is an ubiquitously expressed TF with roles in the transcription of genes essential for embryogenesis (*15*). Re-analysis of the published ADNP ChIP-seq data from mESCs (*15*) showed that ADNP is mostly associated (95%) with REs (fig. S3B). In addition, motif enrichment analysis for ADNP binding in mESCs identified the B-box sequence as the second most represented motif (*15*). Therefore, ADNP could be a strong candidate in helping TFIIIC selective recruitment to the AEs. To test this, we analyzed ADNP ChIP-seq data from human cells (*16*) and found that ADNP is strongly enriched at many TFIIIC-bound AEs (fig. S3C). TAPs were also significantly enriched for ADNP occupancy compared to a random control set of promoters (Fig. 2B). Depleting ADNP in T47D cells (fig, S3,

D and E) decreased more than 50% TFIIIC occupancy at AEs (Fig. 2, C and D) and at TAPs (Fig. 2D and S3F). These data support that ADNP promotes recruitment of TFIIIC to AEs.

As the human TFIIIC complex relieves chromatin-mediated repression (*17*), we asked whether its binding to AEs upon SS was mirrored by an increase in chromatin accessibility. Indeed ATAC-seq data indicated that TFIIIC-bound AEs were more accessible upon SS (Fig. 2E). Searching for the underlying molecular mechanism, we considered increased histone acetylation given that three TFIIIC subunits possess intrinsic histone acetyl transferase (HAT) activity (*17, 18*) and that TFIIIC interacts with the HAT p300/CREB-binding protein (CBP) (*19*). The TFIIIC-bound AEs were positive for two histone acetylation marks, H3K18ac and H3K27ac (Fig. 2F; fig. S4, B and C), but upon SS no changes in H3K27ac were observed at TFIIIC-bound AEs (fig. S4D), whereas H3K18ac markedly increased at TFIIIC-AEs and at TAPs, but not at tRNAs (Fig. 2, F to H; fig. S4A). In fact, around 78% of the TFIIIC-bound AEs and 70% of AEs at TAPs were found significantly acetylated at H3K18 upon SS (Fig. 2I and S4E). Surprisingly, even though H3K18ac and H3K27ac are markers of p300/CBP function *in vivo* (*20, 21*), low levels of p300 were observed at these loci both in T47D as well as T98G cells and these levels decreased upon SS (Fig. 2H and S4F).

We reasoned that the HAT activity of TFIIIC could be responsible for the H3K18ac increase over TFIIIC-bound AEs upon SS. Indeed, the catalytic domain of its largest subunit (GTF3C1) robustly acetylates H3K18 *in vitro* and in HepG2 cells (*22*), and this TFIIIC subunit is enriched in TFIIIC-bound AEs in T47D cells upon SS (fig. S4G). Therefore, we used siRNAs against *GTF3C1*-mRNA to reduced its protein levels (Fig. 2J) and found a dramatic reduction in total

levels of H3K18ac in the depleted cells (Fig. 2K and S4H). Moreover, siRNAs targeting *GTF3C5*-mRNA (fig. S4I) (encoding the fifth largest subunit of TFIIIC) known to de-stabilize the interaction of the whole TFIIIC complex with the B-box (*23*), drastically reduced H3K18ac at two TFIIIC-bound AEs (fig. S4J). These results support direct H3K18 acetylation of AEs by TFIIIC upon SS, and further point to this activity as responsible for the increase in chromatin accessibility in TFIIIC-bound AEs.

Since AEs have been shown to evolve towards proto-enhancer function and the epigenetic state of enhancers participates in forging genome topology and gene expression (*5, 6*), TFIIIC might help in reorganizing the landscape of chromatin loops upon SS. To explore this possibility, we compared genomic contacts by *in nucleo* Hi-C (*24*) and transcript levels by mRNA-seq in T47D cells grown in the presence of absence of serum. Within their own topologically-associated domain (TAD), TFIIIC-bound AEs interacted more frequently with genes whose expression was affected by SS (Fig. 3A). As an example, SS induced the interaction of TFIIIC-bound AE near the cell cycle-regulated TAP gene *FEM1A*, with the *UHRF1* locus located ~150 kb downstream (Fig. 3B, Hi-C data in top panel). Additionally, SS disrupted the interaction of the same AE with the *PLIN4/PLIN5* genes located ~200 kb upstream, whose expression was serum-dependent (Fig. 3B, Hi-C data in top and RNA-seq genome browser tracks in bottom panel). When the interaction scores between all TFIIIC-bound AEs and human TSS were calculated, a significant increase was observed upon SS (fig. S5A), suggesting that AEs-bound TFIIIC reshapes the genomic topology of DNA looping between the AEs of TAPs and those promoters whose expression is affected by SS. To gain insight into the functional meaning of SS-induced TFIIIC-

mediated looping, we searched for transcript changes in serum-starved cells depleted of one of the TFIIIC components (siGTF3C5). TFIIIC depletion led to dysregulation of many transcripts (fig. S5, B and C) and we focused on those differentially-expressed genes that did not exhibit significant changes in the siCTRL cells upon SS (fig. S5D and Table S2): 252 genes were up-regulated and 613 were down-regulated. These two sets of genes were referred to as TFIIIC-repressed genes (TRGs) and TFIIIC-activated genes (TAGs) respectively. Interestingly, GO analysis of TAGs showed enrichment for cell-cycle regulated activity (fig. S5E), in agreement with a recent report in glioblastoma cells (*25*).

To explore the role of TFIIIC on the formation of the intra-TADs loops during SS, we analyzed the Hi-C interactions of TFIIIC-occupied sites with genes whose expression was affected by TFIIIC depletion. We found that TFIIIC binding was significantly enriched in TADs containing TAGs compared to those containing TRGs (Fig. 3D), suggesting that TFIIIC-bound AEs could act as rescue modules to prevent drastic repression of TAGs upon SS. In agreement with this, we found that during SS more than 30% (193) of the TAGs contacted an AE bound by TFIIIC and named this subset TGAPs, representing the set of genes that can be co-regulated by local and by long-range interactions with a TFIIIC-bound AE (Fig. 3E). We predicted that TGAPs should also be differentially expressed between normal and serum-deprived conditions. Indeed, the vast majority (~70%) of these genes corresponded to cell cycle-related genes down-regulated by SS, which further lowered their expression upon TFIIIC depletion (Fig. 3F). These results suggest that during SS TFIIIC is required to sustain basal transcription levels of a subset of genes with cell cycle functions.

We then asked how TFIIIC could promote chromatin looping. CTCF is enriched at promoter regions (*26*), and has been shown to interact with TFIIIC (*27*). Notably, CTCF occupancy at TGAPs was significantly higher compared to a random set of promoters of the same size (fig. S6, A and B). Co-immunoprecipitation experiments showed a marked increase of TFIIIC interaction with CTCF-containing complexes upon SS (Fig. 3G), which was not due to changes in total TFIIIC protein levels (fig. S6C). The increased interaction between the two insulators upon SS, was also reflected by the Hi-C data with significantly higher level of intra-TAD contacts between the two factors (Fig. 3H), supporting a role of CTCF in facilitating TFIIIC-mediated looping upon SS.

The data so far suggest that TFIIIC depletion should decrease the frequency of interactions upon SS. Indeed, we found that the overall intra-TAD contacts were reduced in siGTF3C5 treated cells compared to the siCTRL treatment (Fig. 4, A and B). Moreover, Hi-C contact counts were also increased upon TFIIIC depletion at the *PLIN4/5* locus (Fig. 4C), resembling the situation observed in the presence of serum (Fig. 3B). It is tempting to speculate that TFIIIC fulfills this role by directly increasing H3K18ac at AEs, and thereby creating an acetylated “transcription-favorable” environment for the target genes, perhaps promoting the spreading of the acetylated mark at distal regions. If so, H3K18ac should also increase at promoters of distant interacting genes upon SS. In support of this proposal, we found that almost 70% of the TGAPs exhibited increase H3K18ac upon SS (Figure 4D). We indeed found that SS caused a drastic change in the overall profile of H3K18ac (but not H3K27ac) at promoter regions. A larger fraction of promoters showed H3K18ac more evenly distributed along a broader region both up- and down-

stream of the TSS (Fig. 4E and fig. S6D). All together these data allow us to link TFIIIC to changes in genome topology and epigenetic marks to maintain mRNA steady state levels of its cell cycle-regulated target genes in response to SS.

One possible outcome of the scenario we proposed is that TFIIIC is also necessary to enable TAGs (Fig. 3C) to quickly respond to serum. RNA-seq analysis of SS cells at various time points after serum re-exposure showed that TAGs rapidly responded to serum addition and increased their expression as soon as 3 h post-addition (Fig. 4F). However, depletion of TFIIIC completely abrogated this transcriptional response (Fig. 4F and S6E). These results support a positive role of TFIIIC-bound AEs in the serum-induced expression of cell cycle-related genes. To show that the AEs are needed for this role of TFIIIC, we used CRISPR-Cas9 technology (*28*) to delete the AE bound by TFIIIC between the *PLIN4/5* and *UHRF1* loci (Fig. 3B; fig. S7, A and B; and supplementary materials and methods). This AE contacts the *UHRF1* locus upon SS (Fig. 3B), and depletion of TFIIIC causes a drastic decrease in its expression during SS (Fig. 3B, genome browser in bottom panel). From the CRISPR/Cas9-based genetic modification of T47D cells we were only able to obtain clones with one modified allele and we chose one of the heterozygous clones for further analysis (fig. S7B). Remarkably, deletion of the AE in just one allele caused almost 50% decrease in the expression of *UHRF1* upon SS, compared to the parental cell line (Fig. 4G). This result agrees with that from TFIIIC depletion in SS (Fig. 3C) and with the Hi-C data (Fig. 3B and 4C), and supports the requirement of the AE to maintain steady-state levels of *UHRF1* transcripts during conditions of stress.

The characterization of the molecular action of a human insulator in governing genome structure and expression during stress conditions was missing so far. Here, we uncover chromatin-associated regulatory mechanisms of cell adaptation to starvation that involve the cooperation of previously unconnected *trans*- and *cis*-elements. Upon SS, the insulator/general transcription factor TFIIIC binds a subset of AEs occupied by ADNP to alter chromatin accessibility and looping to ensure the basal transcription of cell cycle genes, and their full reactivation upon serum re-exposure. The HAT activity of TFIIIC directly acetylates H3K18 at AEs and facilitates their contact with distal CTCF sites near other cell cycle genes promoters, which also become hyperacetylated, thus retaining a low level of expression and its capacity to rapidly respond to serum exposure. Of note, solid tumors have regions with poor blood supply and growth factor starvation (*11*), and we found that the expression of the genes regulated by TFIIIC in response to serum predicts clinical outcome of breast cancer patients (fig. S7, C to E). Therefore, our study ultimately could potentially illuminate new avenues to target TFIIIC for clinical intervention.

References

1. T. I. Lee, R. A. Young, Transcriptional regulation and its misregulation in disease. *Cell* **152**, 1237-1251 (2013).
2. A. Pombo, N. Dillon, Three-dimensional genome architecture: players and mechanisms. *Nat Rev Mol Cell Biol* **16**, 245-257 (2015).
3. E. B. Chuong, N. C. Elde, C. Feschotte, Regulatory activities of transposable elements: from conflicts to benefits. *Nat Rev Genet* **18**, 71-86 (2017).
4. A. Cournac, R. Koszul, J. Mozziconacci, The 3D folding of metazoan genomes correlates with the association of similar repetitive elements. *Nucleic Acids Res* **44**, 245-255 (2016).
5. H. J. G. van de Werken *et al.*, Small chromosomal regions position themselves autonomously according to their chromatin class. *Genome Res* **27**, 922-933 (2017).
6. M. Su, D. Han, J. Boyd-Kirkup, X. Yu, J. D. Han, Evolution of Alu elements toward enhancers. *Cell Rep* **7**, 376-385 (2014).
7. D. Filer *et al.*, RNA polymerase III limits longevity downstream of TORC1. *Nature* **552**, 263-267 (2017).
8. G. Dieci, G. Fiorino, M. Castelnuovo, M. Teichmann, A. Pagano, The expanding RNA polymerase III transcriptome. *Trends Genet* **23**, 614-622 (2007).
9. D. Donze, Extra-transcriptional functions of RNA Polymerase III complexes: TFIIIC as a potential global chromatin bookmark. *Gene* **493**, 169-175 (2012).
10. S. Pirkmajer, A. V. Chibalin, Serum starvation: caveat emptor. *Am J Physiol Cell Physiol* **301**, C272-279 (2011).
11. D. Anastasiou, Tumour microenvironment factors shaping the cancer metabolism landscape. *Br J Cancer* **116**, 277-286 (2017).
12. E. Lesniewska, M. Boguta, Novel layers of RNA polymerase III control affecting tRNA gene transcription in eukaryotes. *Open Biol* **7**, (2017).
13. E. A. Bennett *et al.*, Active Alu retrotransposons in the human genome. *Genome Res* **18**, 1875-1883 (2008).
14. Z. Moqtaderi *et al.*, Genomic binding profiles of functionally distinct RNA polymerase III transcription complexes in human cells. *Nat Struct Mol Biol* **17**, 635-640 (2010).
15. V. Ostapcuk *et al.*, Activity-dependent neuroprotective protein recruits HP1 and CHD4 to control lineage-specifying genes. *Nature* **557**, 739-743 (2018).
16. E. P. Consortium, An integrated encyclopedia of DNA elements in the human genome. *Nature* **489**, 57-74 (2012).
17. T. K. Kundu, Z. Wang, R. G. Roeder, Human TFIIIC relieves chromatin-mediated repression of RNA polymerase III transcription and contains an intrinsic histone acetyltransferase activity. *Mol Cell Biol* **19**, 1605-1615 (1999).
18. Y. J. Hsieh, T. K. Kundu, Z. Wang, R. Kovelman, R. G. Roeder, The TFIIIC90 subunit of TFIIIC interacts with multiple components of the RNA polymerase III machinery and contains a histone-specific acetyltransferase activity. *Mol Cell Biol* **19**, 7697-7704 (1999).

19. C. Mertens, R. G. Roeder, Different functional modes of p300 in activation of RNA polymerase III transcription from chromatin templates. *Mol Cell Biol* **28**, 5764-5776 (2008).
20. R. Ferrari *et al.*, Epigenetic reprogramming by adenovirus e1a. *Science* **321**, 1086-1088 (2008).
21. Q. Jin *et al.*, Distinct roles of GCN5/PCAF-mediated H3K9ac and CBP/p300-mediated H3K18/27ac in nuclear receptor transactivation. *EMBO J* **30**, 249-262 (2011).
22. M. B. Basu, R.; Das, S.; Kundu, T. K., The Largest Subunit of Human TFIIIC Complex, TFIIIC220, a Lysine Acetyltransferase Targets Histone H3K18. *BioRxiv*, (2019).
23. S. Jourdain, J. Acker, C. Ducrot, A. Sentenac, O. Lefebvre, The tau95 subunit of yeast TFIIIC influences upstream and downstream functions of TFIIIC.DNA complexes. *J Biol Chem* **278**, 10450-10457 (2003).
24. S. S. Rao *et al.*, A 3D map of the human genome at kilobase resolution reveals principles of chromatin looping. *Cell* **159**, 1665-1680 (2014).
25. G. Buchel *et al.*, Association with Aurora-A Controls N-MYC-Dependent Promoter Escape and Pause Release of RNA Polymerase II during the Cell Cycle. *Cell Rep* **21**, 3483-3497 (2017).
26. M. Ruiz-Velasco *et al.*, CTCF-Mediated Chromatin Loops between Promoter and Gene Body Regulate Alternative Splicing across Individuals. *Cell Syst* **5**, 628-637 e626 (2017).
27. G. G. Galli *et al.*, Genomic and proteomic analyses of Prdm5 reveal interactions with insulator binding proteins in embryonic stem cells. *Mol Cell Biol* **33**, 4504-4516 (2013).
28. H. Wang, M. La Russa, L. S. Qi, CRISPR/Cas9 in Genome Editing and Beyond. *Annu Rev Biochem* **85**, 227-264 (2016).
29. M. Ringner, E. Fredlund, J. Hakkinen, A. Borg, J. Staaf, GOBO: gene expression-based outcome for breast cancer online. *PLoS One* **6**, e17911 (2011).

Notes

Acknowledgments

We would like to thank all the members of the Beato's lab, the CRG Gene Regulation, Stem Cells and Cancer Program, the CRG Genome Facility, the 4D Genome Unit of the Synergy program, Jose Luis Villanueva (CRG), Yasmina Cuartero (CRG) and Prof. Simone Ottonello (University of Parma, Italy) for the invaluable source of insight and help.

Funding

Spanish Ministry of Economy and Competitiveness 'Centro de Excelencia Severo Ochoa 2013–2017' [SEV-2012-0208] and BFU2016-76141-P (to S.L.); ACER (to C.R.G.); EMBO Long-term Fellowship (ALTF 1201-2014 to R.F.); Marie Curie Individual Fellowship (H2020-MSCA-IF-2014); European Research Council under the European Union's Seventh Framework Programme (FP7/2007–2013/ERC Synergy grant agreement 609989 [4DGenome]). We acknowledge the support of the CERCA Programme / Generalitat de Catalunya. Funding for open access charge: European Research Council. We also acknowledge the support of the Italian Association for Cancer Research (AIRC, Grant IG16877 to G.D.).

Author Contributions

R.F. and L.I.L.C. and M.B. designed the experiments. R.F., L.I.L.C., C.D.V. and F.D.L. performed the experiments. R.F., E.V., J.Q.O. and A.L. A.L. carried out the biostatistics analysis. F.D.L.

also assisted with the sequencing. R.F. and M.B. wrote the manuscript in consultation with G.D., M.T. A.V. and S.L. M.T. also provided some of the antibodies used in this study.

Declaration of Interests

None declared.

Figure Legends

Figure 1. Reversible TFIIIC occupancy at AEs increases during SS in tumor and non-tumor cells.

(**A-B**) Venn diagram of overlapping peaks in the presence (+S, red) and absence (–S, grey) conditions for TFIIIC and CTCF.

(**C**) Stacked plot for percentage of TFIIIC peaks over AEs, tRNA or other loci in +S or –S conditions.

(**D**) Bar plot showing the increased number of all TFIIIC-bound AEs with a ±5 kb window around all human TSS. Compare –S, grey with +S, red.

(**E**) CEAS plots of ΔTFIIIC average binding at TAPs (red) comparing conditions of +S and –S (+S subtracted from –S). The profile of a random set of genes of the same size of TAPs (purple), as well as the average for all human TSS (black) is also included.

(**F**) Genome browser view of representative cell cycle-regulated locus *HELLS* with ChIP-seq tags counts for TFIIIC in different cell lines (IMR90, T98G, MCF10A and T47D) in the presence (red) or absence (grey) of serum (+/–S). TFIIIC bound to AE is highlighted by a grey rectangle. *HELLS* genomic structure and the direction of transcription (arrow) are shown at the bottom.

(**G**) CEAS plots of TFIIIC average enrichment in T47D cells in conditions of +S, –S and –S followed by serum addition for 30 min (–S/+S30'). The graphs are plotted over the TFIIIC peaks summit in the –S condition (plotted is the –log10 of the Poisson p-value, see methods).

Figure 2. ADNP guides TFIIIC and its GTF3C1 HAT activity to directly acetylate H3K18 at AEs during SS.

(**A**) Area plot ranking (from higher to lower) unique spectral counts (average of three replicates) of major TFIIIC interactors using a GTF3C2 antibody as bait in T47D cells grown in +S and –S conditions. Data from IgG control immunoprecipitations are shown in blue (the bait is in bold). Preys proteins are indicated in black, except for the ones forming the ChAHP complex (purple).

(**B**) Average plot for ADNP-eGFP (GSE105573) enrichment across as TAPs (red) spanning a 6 kb region (±3 kb). Indicated is also the profile of a random set of genes of the same size of TAPs (purple), as well as the average for all human TSS (black).

(**C**) Heatmap of TFIIIC occupancy in control (siCTRL) and ADNP depleted cells (siADNP) ranked for enrichment in the siCTRL sample (left panel). In the siADNP sample TFIIIC occupancy is significantly reduced (right panel). Color bar scales with increasing shades of color stands for higher enrichment (plotted is the –log10 of the Poisson p-value). ADNP depletion levels are shown in fig. S3, C and D.

(**D**) Genome browser view of representative TAPs genes *FEM1A* and *HELLS* showing TFIIIC occupancy in T47D depleted of ADNP (siADNP) compared to control cells (siCTRL). The position of the ADNP binding is represented by the blue track (eGFP-ADNP). The corresponding gene and the direction of transcription (arrow) are shown at the bottom.

(**E**) ATAC-seq signal enrichment in +S and –S conditions across all TFIIIC peak summit in –S condition (plotted is the –log10 of the Poisson p-value).

(**F**) Average profile of H3K18ac enrichment in +S and –S conditions across all TFIIIC-bound AEs (plotted is the –log10 of the Poisson p-value).

(**G**) CEAS plots of H3K18ac average at TAPs (red) in –S condition. The profile of a random set of genes of the same size of TAPs (purple), as well as the average for all human TSS (black) is also included.

(**H**) Genome browser view of representative TAP genes *FEM1A* and *HELLS* with ChIP-seq data for p300 and H3K18ac in T47D +S or -S conditions. Highlighted in grey is the AE bound by TFIIIC for each locus. The corresponding gene and the direction of transcription (arrow) are shown at the bottom. Note that p300 is not recruited at the AEs bound by TFIIIC as it is for other adjacent intergenic regions (yellow rectangle).

(**I**) Venn diagram showing the total number of AEs bound by TFIIIC and those acetylated in H3K18.

(**J**) Immunoblot probing the levels of GTF3C1 protein in cells transfected with siGTF3C1 or siCTRL in SS. Histone H1.2 is shown as loading control.

(**K**) H3K18ac immunostaining (red) of siCTRL and siGTF3C1-transfected T47D cells in SS. DAPI was used to stained nuclei (blue). Two different fields are shown. Scale bar, 100 μm.

Figure 3. Long-range interactions of TFIIIC and CTCF mediate DNA looping for maintaining gene expression patterns during SS.

(**A**) Hi-C analysis of intra-TAD contacts between TFIIIC-bound AEs and gene promoters represented as log2 fold change (FC) (and 95 % confidence interval (CI)) of the contact

enrichment between +S and -S conditions for genes differentially expressed (orange) or not affected (green) upon SS. Posterior probabilities PPr = 0.93 (see methods).

(**B**) Subtraction interaction matrix ΔHi-C (+S matrix is subtracted from the –S matrix) of *PLIN4/5* and *UHRF1* loci for TFIIIC-bound AEs. The regions with changes in their interaction upon SS have been zoomed out to better visualize those regions of preferred interaction (top panel). ChIP-seq and RNA-seq data (A and B indicate two biological replicates) are also reported as genome browser views of the two loci (bottom panel). Grey rectangles highlight the position of the AEs and the genes interacting.

(**C**) Heatmaps of gene expression for siGTF3C5 and siCTRL cells (both in –S). Color bar scale stands for log2FC of normalized RNA expression in each condition compared to cells in the absence of serum. Only the genes that changed their expression significantly in the siGTF3C5-cells, and not in the siCTRL cells are shown. Two classes of genes were designated as TFIIIC-activated genes (TAGs) or TFIIIC-repressed genes (TRGs).

(**D**) TFIIIC contact enrichment of the TAGs and TRGs using Hi-C data in the –S condition. The P-value for logistic regression comparing TAGs and TAPs is reported.

(**E**) Venn diagram of overlap between TAGs (613 genes) and 193 genes bound by TFIIIC directly (within a 10 kb region) or via DNA looping (TGAPs).

(**F**) Heatmaps of the expression of TGAPs for conditions of +S, siGTF3C5 (-S) and siCTRL (-S). Color bar scale stands for log2FC of normalized RNA expression in each condition compared to cells in the absence of serum.

(**G**) Co-immunoprecipitation of CTCF and TFIIIC in soluble T47D cell extracts comparing +S and –S conditions ("beads only" are used as a specificity control). Membranes were probed with anti-CTCF and GTF3C2 antibodies. Input lysates (10%) are also shown.

(**H**) Hi-C analysis of TFIIIC and CTCF contacts represented as log2 FC (and 95 % CI) of the specific CTCF-TFIIIC contact enrichment compared to CTCF and TFIIIC additive effect for both +S and -S conditions. (E=expected by CTCF and TFIIIC additive effect). PPr = 0.83 indicates a high probability of an increase in TFIIIC Hi-C contact with CTCF the -S sample compared to +S.

Figure 4. Impaired DNA looping at TGAPs by TFIIIC depletion abrogates the reactivation of gene expression upon serum re-exposure.

(**A**) Changes in specific intra-TADs contacts made by TFIIIC in +S/-S or siGTF3C5/siCTRL cells. Data is the log2FC of observed *vs* expected (and 95 % CI) of Hi-C data. The changes in siGTF3C5/siCTRL show significant (PPr = 0.99) decrease of total intra-TADs contacts compared to –S/siCTRL.

(**B**) Boxplot of the normalized interaction score of Hi-C data for siCTRL and siGTF3C5 between promoters and TFIIIC-bound AEs for TGAPs Two Hi-C biological replicates were used (p-value from Friedman X^2 test is indicated).

(**C**) Hi-C subtraction matrix of the *UHRF1* locus for siCTRL and siGTF3C5 cells. The siGTF3C5 matrix is subtracted of the siCTRL matrix. Arrow indicates the looping between the AE bound by TFIIIC and its respective targets (*PLIN4/5* or *UHRF1*). The region that changes its interaction upon SS has been zoomed out to better visualize the preferred interactions.

(**D**) Stacked plot representing changes in H3K18ac upon SS in TGAPs. Note that around 70% of them display increased acetylation.

(**E**) Heatmap representation of H3K18ac spanning a 20 kb-region of all human promoters in +S and –S conditions in T47D cells. Biased clustering shows promoters that increased H3K18ac upon SS; this cluster contains several TGAPs.

(**F**) RNA-seq expression analysis of TAGs after serum exposure for the indicated times in conditions of siCTRL and siGTF3C5 in T47D cells. Data is in rpm. Significant p-values from a two-tailed paired Student's *t*-test are reported in comparisons for each time-point. The comparison between 0 to 3 h in siCTRL cells is shown to highlight the rapidity of gene activation after serum addition. *** $p < 1.0E10^{-20}$, ** $p < 1.0E10^{-12}$. GTF3C5 depleted levels were maintained during the time course (fig. S6F).

(**G**) *UHRF1* expression by qRT-PCR in T47D parental cells (WT) and AE-CRISPR/Cas9-Clone11 in the absence of serum (mean ± SEM of 2 biological replicates; data in WT cells have been normalized to 1). One tail *t*-test p-value is indicated.

Supplementary Figure Legends

Figure S1. TFIIIC (but not TFIIIB or Pol III) binds to AEs close to Pol II promoters of cell cycle-enriched genes upon SS.

(**A**) Schematic view of experimental design.

(**B**) Fraction of T47D cells at the indicated phases of the cell cycle.

(**C**) Word cloud analysis of RE bound by TFIIIC in the presence (+S) or absence (-S) serum.

(**D**) Proportional Venn diagram of total AEs bound by TFIIIC detected in SS *vs* ETC sites (with only B-box).

(**E**) Bar plots of gene ontology (GO) enrichment as calculated by DAVID GO (Molecular Function and Biological Processes combined) for TAPs genes. GO terms are ranked from the lowest to the highest P-value of the first nine terms found by DAVID GO.

(**F**) CEAS plots of BDP1 (left) and RPC39/Pol III (right) average binding to AEs bound by TFIIIC (top panels) tRNA genes (bottom panels) in condition of +S and -S (plotted is the –log10 of the Poisson p-value).

(**G**) Heatmap of AE density across all human TSS spanning a 6 kb region (±3 kb), and sorted by high to low AE density. TAPs, which correspond to Pol II promoters with TFIIIC-bound, are shown at the top. Color bar scale with increasing shades of color stands for higher AE density.

Figure S2. TFIIIC binding in different cell lines shows increased AEs occupancy upon SS.

(**A**) CEAS plot of TFIIIC average binding in condition of +S and –S over peaks detected in the –S condition in MCF10A, T98G and IMR90 cells (plotted is the –log10 of the Poisson p-value). The enrichment in peaks corresponds to AEs.

(**B**) Genome browser view of *CCNE1, MDM4 and UBE2V2* loci with ChIP-seq data for Pol III, BDP1 and TFIIIC in MCF10A and T47D breast cell lines. The graph includes the tracks for AEs and tRNA genes. Highlighted in grey is the AE bound by TFIIIC in the two cell lines close to the TSS of the genes indicated.

(**C**) CEAS plots of TFIIIC average enrichment in conditions of +S, –S and –S followed by serum addition for 30 min (–S/+S30') for T98G cells. The graphs are plotted over TFIIIC peaks summit in the –S condition (plotted is the –log10 of the Poisson p-value).

Figure S3. ADNP interacts with TFIIIC and binds AEs occupied by TFIIIC upon SS.

(A) Direct interaction of recombinant ADNP and TFIIIC. Flag-tagged TFIIIC or HA-tagged ADNP were expressed by baculovirus infection of insect cells. For TFIIIC expression, cells were co-infected with baculo-vectors to expressed Flag-tagged GTF3C1 and the rest of the TFIIIC subunits untagged. Note that immunopurification via the Flag-tag brings down the whole TFIIIC complex. GTF3C5 fractionates on top of the heavy IgG chain. **Left Panel**: Coomassie staining of anti-Flag immuno-purifications of lysates expressing TFIIIC, ADNP or both together. A substantial amount of ADNP co-purifies with TFIIIC. **Right Panel**: Coomassie staining of anti-HA immuno-purifications of lysates expressing HA-ADNP alone or together with TFIIIC. The

presence of the TFIIIC subunits is clearly detected in the ADNP immuno-complexes. The asterisks indicate the IgG heavy and light chains. The identity of the bands was confirmed by mass-spectrometry.

(**B**) Pie chart showing the percentage of mouse Adnp peaks belonging to RE and non-RE (GSE97945). Notice that almost all the binding of this factor lays on RE.

(**C**) Heatmap of ADNP-eGFP binding in K562 cells spanning ±1 kb across all TFIIIC-bound AEs in T47D (GSE105573). AEs are ranked from high to low ADNP-eGFP enrichment. Color bar scale with increasing shades of color stands for higher enrichment (plotted is the –log10 of the Poisson p-value).

(**D**) qRT-PCR expression analysis of *ADNP* in T47D cells (siCTRL and siADNP) during SS corresponding to the experiment in Fig. 2C. The value in siCTRL cells was arbitrarily set as 1. Note that the knockdown of *ADNP* reaches values almost 80% of its control.

(**E**) Immunoblot probing the levels of ADNP protein in cells transfected with siADNP or control siCTRL in SS conditions. Histone H1.2 is shown as loading control.

(**F**) CEAS profile of TFIIIC enrichment over TAPs upon depletion of ADNP (siADNP) compared to control cells (siCTRL). Notice the reduced TFIIIC occupancy at these genes in ADNP knocked down cells.

Figure S4. H3K18ac but not H3K27ac marks AEs occupied by TFIIIC upon SS.

(**A**) Sitepro profile of H3K18ac enrichment in +S and –S at tRNA genes (plotted is the –log10 of the Poisson p-value).

(**B-C**) CEAS profile of H3K27ac enrichment at TAPs. The profile of a random set of genes of the same size of TAPs (purple), as well as the average for all human TSS (black) is also included (plotted is the –log10 of the Poisson p-value). Notice that H3K27ac is more enriched at TAPs (red) than on a control set of random promoters (purple), but remains unchanged upon SS (comparison in fig. S4D).

(**D**) Sitepro profile of H3K27ac enrichment in +S and –S over TFIIIC-bound AEs (plotted is the –log10 of the Poisson p-value). H3K27ac levels at these sites are independent of SS.

(**E**) Proportional Venn diagram showing the total number of TAPs and those enriched in H3K18ac in the absence of serum.

(**F**) Average plot for p300 occupancy in T47D (left panel) and T98G (right panel) across all TFIIIC-bound AEs spanning a 6 kb region (±3 kb) in the presence (+S, red) or absence (-S, grey) of serum. T98G p300 data was from (GSE21026).

(**G**) Average plot for GTF3C1 occupancy in T47D enrichment across all TFIIIC-bound AEs spanning a 6-kb region (±3 kb) in –S condition.

(**H**) Histogram plot of Pearson's correlations frequency of H3K18ac colocalization with DAPI staining of figure 2K. The large majority of cells in the siCTRL had H3K18ac colocalizing with DAPI, whereas cellular ablation of GTF3C1 caused the loss of H3K18ac and consequently its colocalization with DAPI.

(**I**) Immunoblot probing the levels of GTF3C5 protein in T47D cells transfected with siGTF3C5 or control siCTRL used in panel H.

(**J**) ChIP-qPCR showing loss of H3K18ac enrichment at two AEs bound by TFIIIC (*UHRF1* and *HELLS* loci) in SS upon knock down of *GTF3C5* by siRNA. The graph shows the mean and SD of 2 independent experiments.

Figure S5. Global Gene expression analysis of T47D before and after SS and in condition of TFIIIC depletion.

(**A**) Box plot of oneD-normalized interaction scores calculated for all the AEs bound by TFIIIC for condition of +S and -S. Note the significant increased interaction score upon SS (Kolmogorov-Smirnov Test < 0.001).

(**B**) Volcano plot comparing mRNA-seq data of siGTF3C5 *vs* siCTRL in -S conditions (plotted the –log10 of the p-value *vs* the -log2 ratio of siGTF3C5 *vs* siCTRL). The genes that scored significant (p-value < 0.05) are indicated in red (FC>1.5) and blue (FC<-1.5). *GTF3C5* is found among the most downregulated genes. See Table S2 for more information.

(**C-D**) Scatter plot of gene expression comparing siGTF3C5 (C) and siCTRL (D) treated cells (–S) *vs* –S condition. The number of genes up- or down-regulated (-1.5 < FC > 1.5; p-value < 0.05) is indicated in red or blue, respectively.

(**E**) Bar plots of GO enrichment of TAGs.

Figure S6. Upon SS, interaction of TFIIIC and CTCF might generate a hyper-acetylated environment by acetylating H3K18 at AEs of TAPs and promoters of TGAPs.

(**A**) Boxplot of CTCF significant binding events within a 10 kb region around TSS of TGAPs, or of a random dataset of TSS of the same size. P-value of a Friedman X^2 test is indicated.

(**B**) Genome browser view of representative cell cycle-related TAGs *CCND1, CCNF, CENPE and POLQ*, for ChIP-seq data of CTCF and TFIIIC in T47D in +S and –S conditions. The multiple CTCF peaks are highlighted with grey boxes. Note that multiple CTCF binding sites are present at the 5' end of the *CCNF* gene. Transcription directionality is indicated.

(**C**) Western blot of different TFIIIC subunits (GTF3C1, GTF3C2, GTF3C4 and GTF3C5) in +S and –S conditions. For each panel, a loading control with Tubulin is also shown.

(**D)** CEAS plot of H3K18ac and H3K27ac average at the TSS of all human genes in +S or –S conditions in T47D cells (plotted is the –log10 of the Poisson p-value). Note how H3K18ac is drastically changed upon SS in comparison with H3K27ac, which remains unaffected.

(**E**) qRT-PCR expression analysis of *GTF3C5* in T47D cells (siCTRL and siGT3C5) released from SS by serum addition for the indicated times. Graph represents the mean ± SEM from two biological experiments, in which the value in siCTRL cells was arbitrarily set as 1 at each time point. Note that the knockdown of TFIIIC always reaches values of more than 70% at each time point analyzed.

Figure S7. AE deletion affects DNA looping and expression of distal *UHRF1* locus.

(**A**) Schematic representation of the CRISPR-Cas9 approach to delete the TFIIIC-bound AE located between the *PLIN4/5* and *UHRF1* loci in chromosome 17. The wild-type (WT) and the deleted alleles are shown. The targeted AE is shown as a purple box, the position of the guide RNAs (gRNA1 and gRNA2) is marked with triangles, and the primers used for the screen (see panel B) are indicated with blue arrows. Arrows indicate the chromatin interactions in +S and -S conditions (red and black, respectively), based on Fig. 3B.

(**B**) PCR result for the screen of CRISPR-Cas9 T47D clones with primers Up3 and Down (see supplementary materials and methods for details): the upper band corresponds to the WT allele, whereas the lower band correspond to the deleted allele. Representative clones are shown, but almost all clones analyzed were heterozygous for the deletion. For further analysis, clone 11 was selected. The DNA marker size is shown. * indicates a non-specific band. NC corresponds to no DNA sample.

(**C-D**) Kaplan–Meier plots of breast tumor samples for TAPs or TAGs expression, respectively. TAPs genes were divided in three main groups according to their expression levels within brackets (with blue being the highest, red the intermediate and grey the lowest). P-values from a Mantel-Cox test are indicated. Higher expression of TAPs is associated with poor prognosis for overall survival and distance metastasis free survival (DMFS), respectively. Plots are generated using (GOBO) (*29*).

(**E**) Boxplots of expression of TAPs from all tumor samples across the three breast cancer grades. Box plots are generated by using (GOBO). TAPs show higher expression in most aggressive tumors (3rd grade), p-value is also indicated.

Figure 1

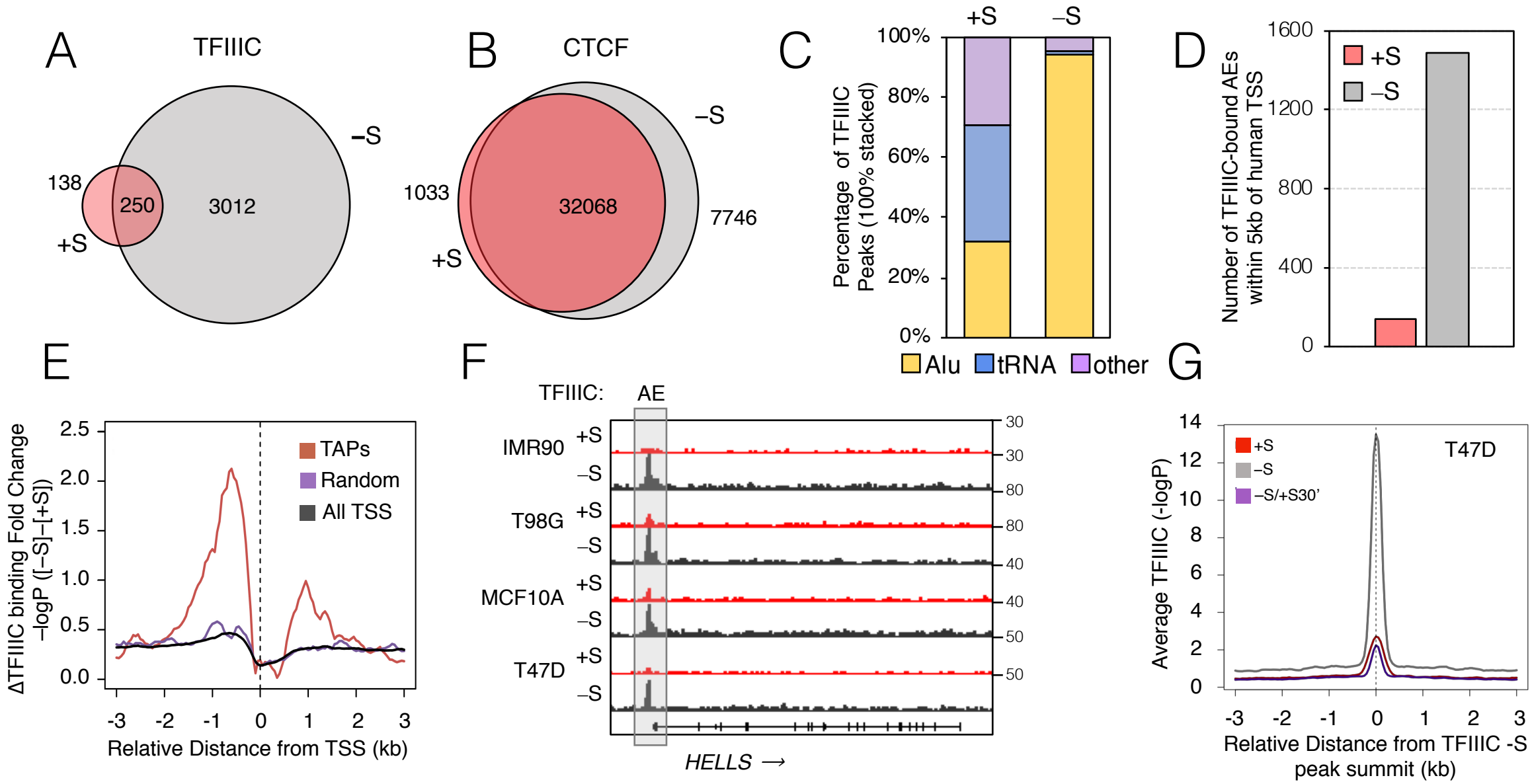
A
TFIIIC
138
250
3012
+S
–S
B
CTCF
1033
32068
7746
+S
–S
C
+S
–S
Percentage of TFIIIC Peaks (100% stacked)
100%
80%
60%
40%
20%
0%
Alu
tRNA
other
D
Number of TFIIIC-bound AEs within 5kb of human TSS
1600
1200
800
400
0
+S
–S
E
ΔTFIIIC binding Fold Change −logP ([–S]–[+S])
2.5
2.0
1.5
1.0
0.5
0.0
TAPs
Random
All TSS
-3
-2
-1
0
1
2
3
Relative Distance from TSS (kb)
F
TFIIIC:
AE
IMR90
T98G
MCF10A
T47D
+S
–S
30
30
80
80
40
40
50
50
HELLS →
G
Average TFIIIC (-logP)
14
12
10
8
6
4
2
0
+S
–S
–S/+S30'
T47D
-3
-2
-1
0
1
2
3
Relative Distance from TFIIIC -S peak summit (kb)

Figure 2

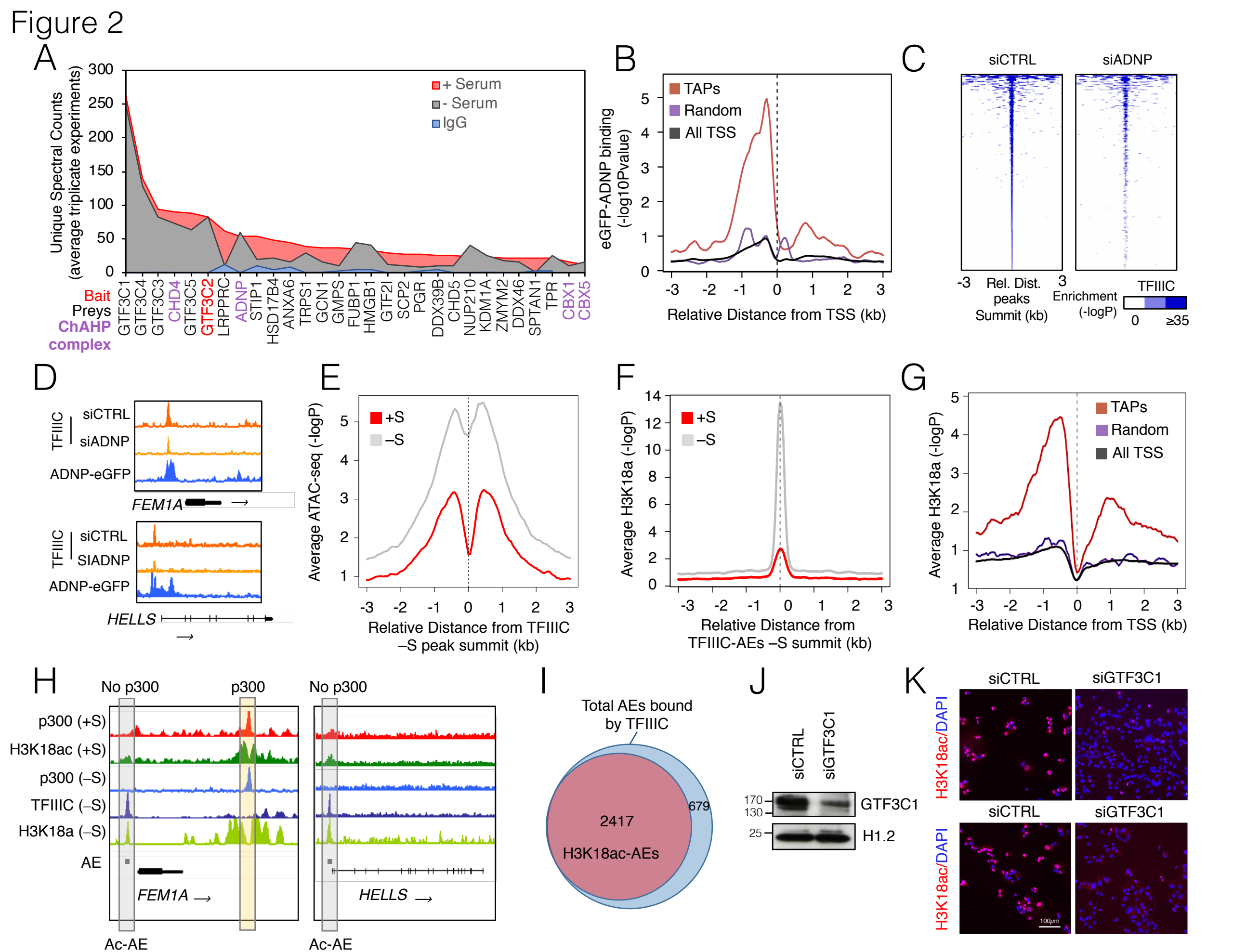
A
Unique Spectral Counts (average triplicate experiments)
+ Serum
- Serum
IgG
Bait
Preys
ChAHP complex
GTF3C1 GTF3C4 GTF3C3 CHD4 GTF3C5 GTF3C2 LRPPRC ADNP STIP1 HSD17B4 ANXA6 TRPS1 GCN1 GMPS FUBP1 HMGB1 GTF2I SCP2 PGR DDX39B CHD5 NUP210 KDM1A ZMYM2 DDX46 SPTAN1 TPR CBX1 CBX5
B
eGFP-ADNP binding (-log10Pvalue)
TAPs
Random
All TSS
Relative Distance from TSS (kb)
C
siCTRL
siADNP
Rel. Dist. peaks Summit (kb)
Enrichment (-logP)
TFIIIC
0
≥35
D
TFIIIC
siCTRL
siADNP
ADNP-eGFP
FEM1A
siCTRL
SIADNP
ADNP-eGFP
HELLS
E
Average ATAC-seq (-logP)
+S
–S
Relative Distance from TFIIIC –S peak summit (kb)
F
Average H3K18a (-logP)
+S
–S
Relative Distance from TFIIIC-AEs –S summit (kb)
G
Average H3K18a (-logP)
TAPs
Random
All TSS
Relative Distance from TSS (kb)
H
No p300
p300
No p300
p300 (+S)
H3K18ac (+S)
p300 (–S)
TFIIIC (–S)
H3K18a (–S)
AE
FEM1A
HELLS
Ac-AE
Ac-AE
I
Total AEs bound by TFIIIC
2417
H3K18ac-AEs
679
J
siCTRL
siGTF3C1
170
130
GTF3C1
25
H1.2
K
siCTRL
siGTF3C1
H3K18ac/DAPI
siCTRL
siGTF3C1
H3K18ac/DAPI
100μm

Figure 3

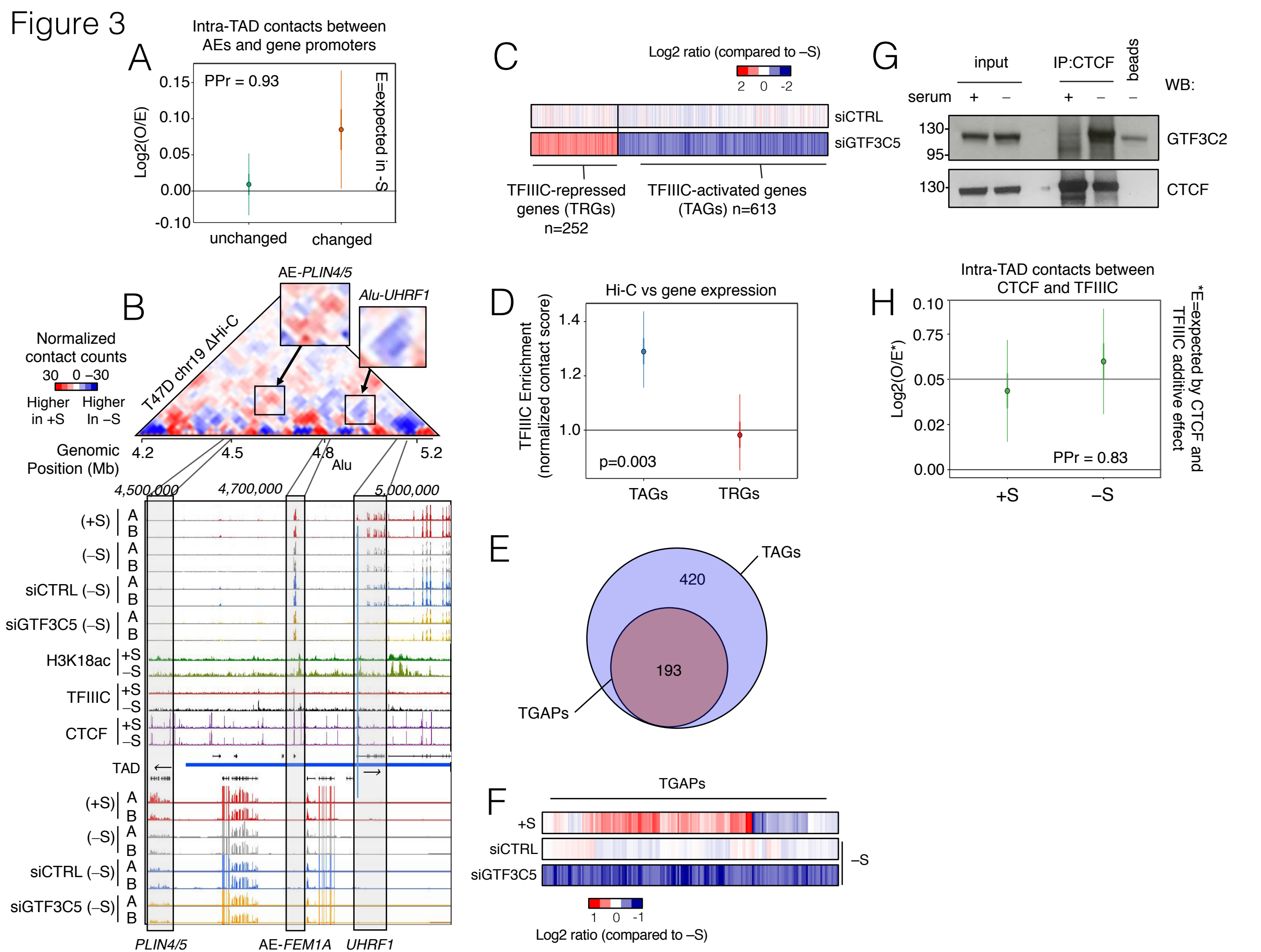
A
Intra-TAD contacts between AEs and gene promoters
PPr = 0.93
Log2(O/E)
E=expected in -S
unchanged
changed
B
AE-PLIN4/5
Alu-UHRF1
T47D chr19 ΔHi-C
Normalized contact counts
30 0 −30
Higher in +S
Higher In −S
Genomic Position (Mb)
4.2
4.5
4.8
5.2
Alu
4,500,000
4,700,000
5,000,000
(+S)
(−S)
siCTRL (−S)
siGTF3C5 (−S)
H3K18ac
TFIIIC
CTCF
TAD
PLIN4/5
AE-FEM1A
UHRF1
C
Log2 ratio (compared to −S)
2 0 -2
siCTRL
siGTF3C5
TFIIIC-repressed genes (TRGs) n=252
TFIIIC-activated genes (TAGs) n=613
D
Hi-C vs gene expression
TFIIIC Enrichment (normalized contact score)
p=0.003
TAGs
TRGs
E
TAGs
420
193
TGAPs
F
TGAPs
+S
siCTRL
siGTF3C5
−S
1 0 -1
Log2 ratio (compared to −S)
G
input
IP:CTCF
beads
WB:
serum
GTF3C2
CTCF
H
Intra-TAD contacts between CTCF and TFIIIC
Log2(O/E*)
PPr = 0.83
*E=expected by CTCF and TFIIIC additive effect
+S
−S

Figure 4

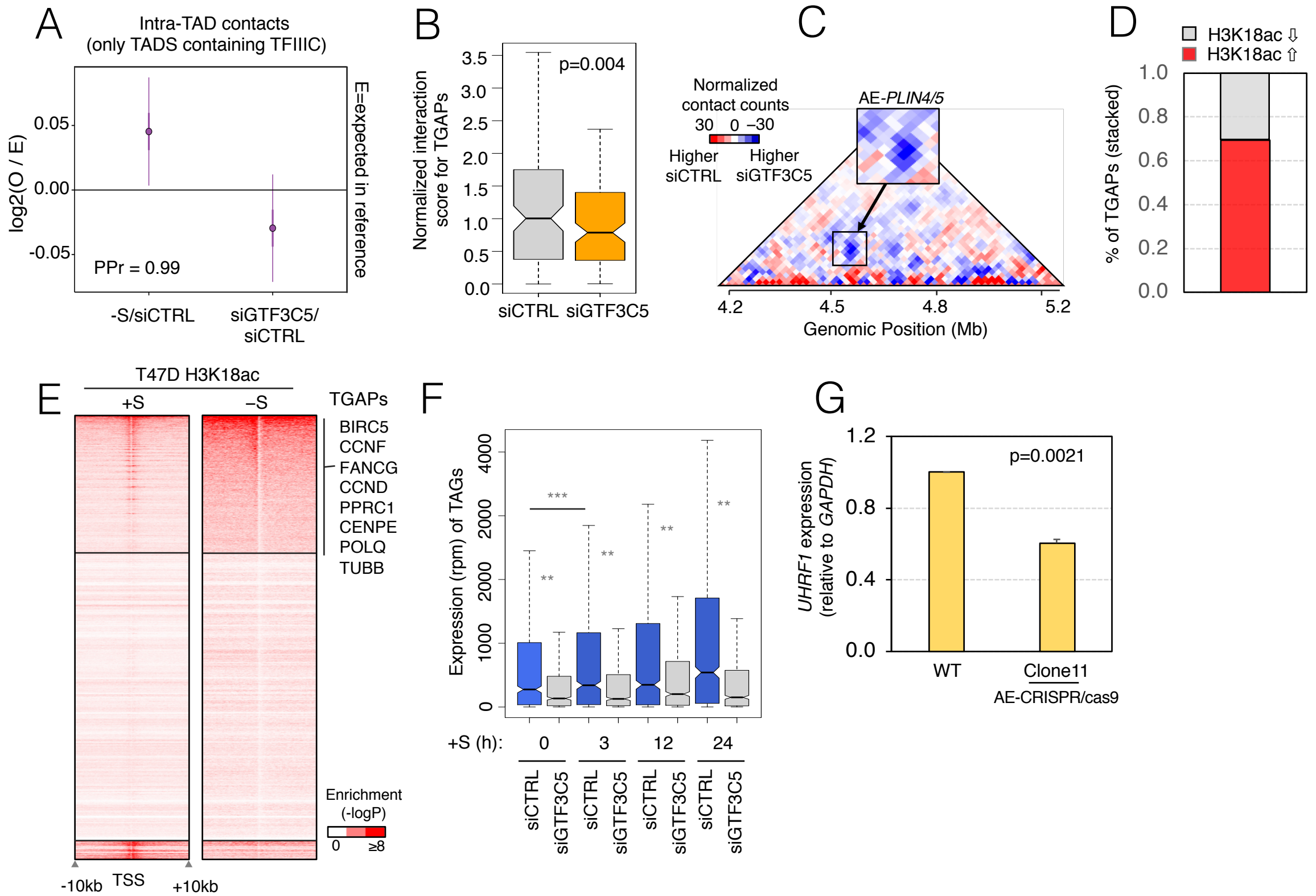
A
Intra-TAD contacts
(only TADS containing TFIIIC)
log2(O / E)
0.05
0.00
-0.05
PPr = 0.99
-S/siCTRL
siGTF3C5/
siCTRL
E=expected in reference
B
Normalized interaction
score for TGAPs
p=0.004
3.5
3.0
2.5
2.0
1.5
1.0
0.5
0.0
siCTRL
siGTF3C5
C
Normalized
contact counts
30 0 −30
Higher
siCTRL
Higher
siGTF3C5
AE-PLIN4/5
4.2
4.5
4.8
5.2
Genomic Position (Mb)
D
H3K18ac ⇩
H3K18ac ⇧
% of TGAPs (stacked)
1.0
0.8
0.6
0.4
0.2
0.0
E
T47D H3K18ac
+S
−S
TGAPs
BIRC5
CCNF
FANCG
CCND
PPRC1
CENPE
POLQ
TUBB
Enrichment
(-logP)
0
≥8
-10kb
TSS
+10kb
F
Expression (rpm) of TAGs
4000
2000
2000
1000
0
***
**
**
**
**
+S (h):
0
3
12
24
siCTRL
siGTF3C5
siCTRL
siGTF3C5
siCTRL
siGTF3C5
siCTRL
siGTF3C5
G
UHRF1 expression
(relative to GAPDH)
1.2
0.8
0.4
0.0
p=0.0021
WT
Clone11
AE-CRISPR/cas9

Fig. S1

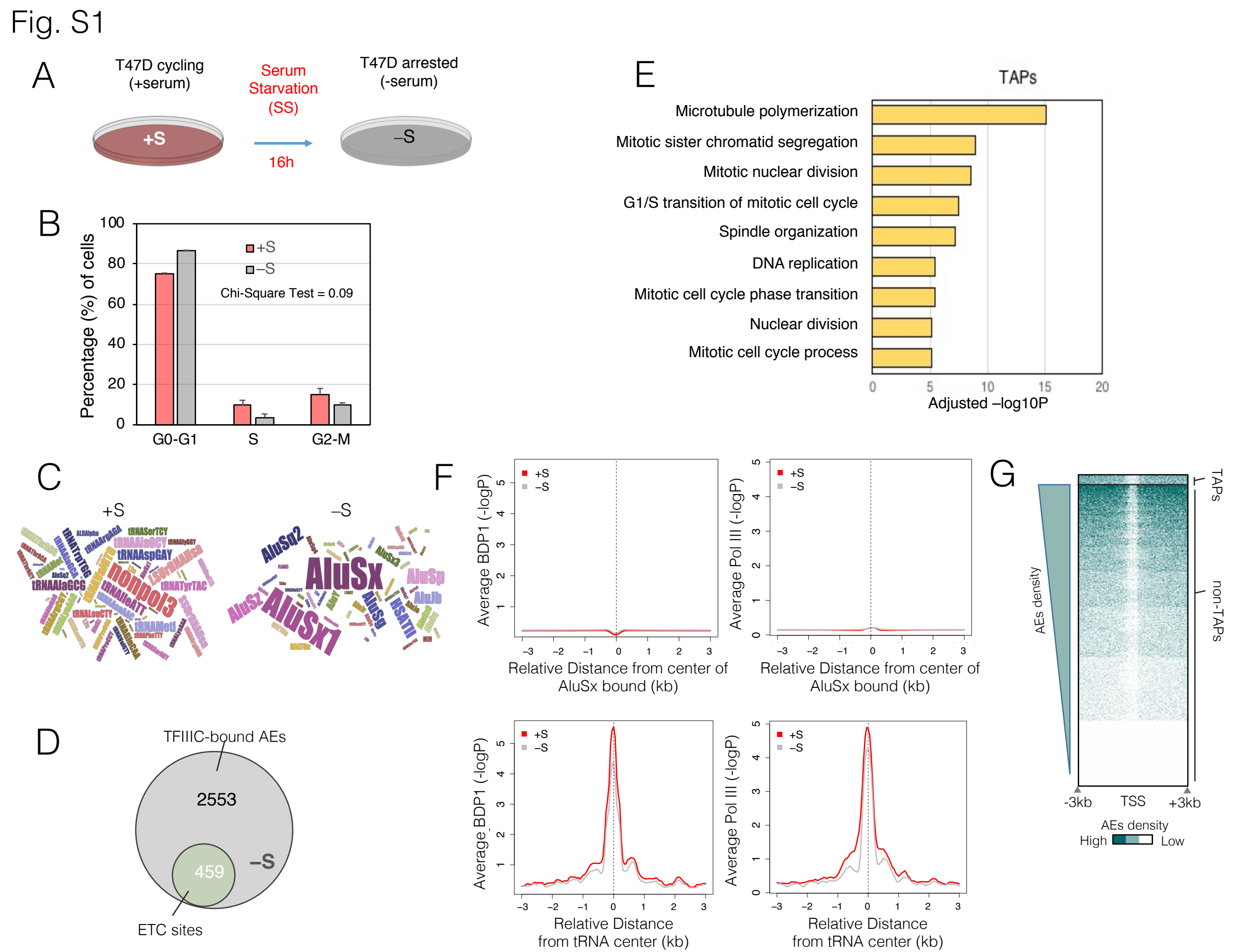
A
T47D cycling
(+serum)
Serum
Starvation
(SS)
T47D arrested
(-serum)
+S
–S
16h
B
Percentage (%) of cells
100
80
60
40
20
0
+S
–S
Chi-Square Test = 0.09
G0-G1
S
G2-M
C
+S
–S
nonpol3
AluSx
AluSx1
AluSq2
AluSp
AluJb
AluSg
MSATII
D
TFIIIC-bound AEs
2553
459
–S
ETC sites
E
TAPs
Microtubule polymerization
Mitotic sister chromatid segregation
Mitotic nuclear division
G1/S transition of mitotic cell cycle
Spindle organization
DNA replication
Mitotic cell cycle phase transition
Nuclear division
Mitotic cell cycle process
0
5
10
15
20
Adjusted –log10P
F
Average BDP1 (-logP)
Average Pol III (-logP)
+S
–S
Relative Distance from center of
AluSx bound (kb)
Relative Distance
from tRNA center (kb)
G
AEs density
TAPs
non-TAPs
-3kb
TSS
+3kb
AEs density
High
Low

Fig. S2

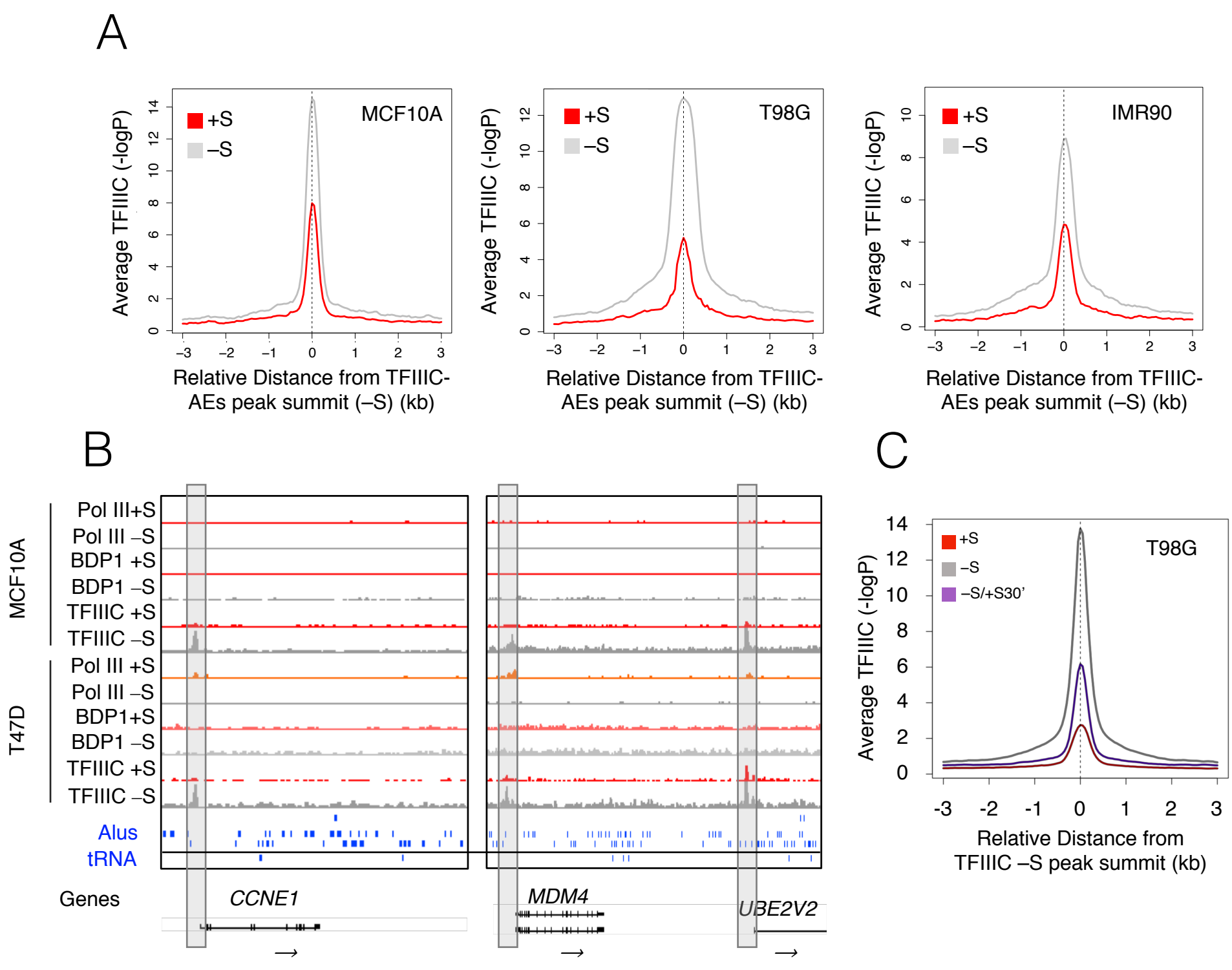
A
MCF10A
T98G
IMR90
+S
–S
Average TFIIIC (-logP)
Relative Distance from TFIIIC-AEs peak summit (–S) (kb)
B
MCF10A
T47D
Pol III+S
Pol III –S
BDP1 +S
BDP1 –S
TFIIIC +S
TFIIIC –S
Pol III +S
Pol III –S
BDP1+S
BDP1 –S
TFIIIC +S
TFIIIC –S
Alus
tRNA
Genes
CCNE1
MDM4
UBE2V2
C
T98G
+S
–S
–S/+S30'
Average TFIIIC (-logP)
Relative Distance from TFIIIC –S peak summit (kb)

Fig. S3

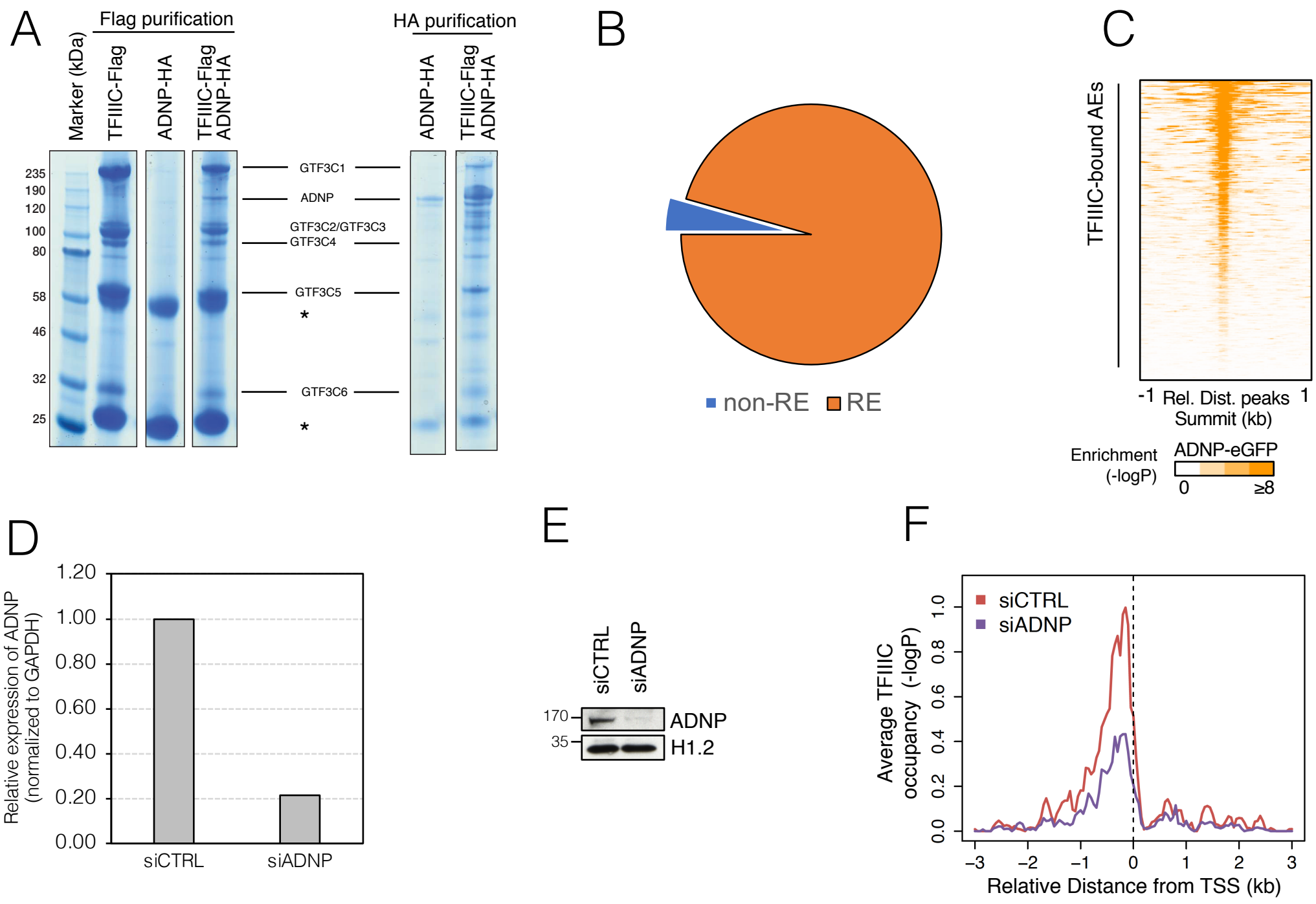
A
Flag purification
HA purification
Marker (kDa)
TFIIIC-Flag
ADNP-HA
TFIIIC-Flag ADNP-HA
ADNP-HA
TFIIIC-Flag ADNP-HA
235
190
120
100
80
58
46
32
25
GTF3C1
ADNP
GTF3C2/GTF3C3
GTF3C4
GTF3C5
*
GTF3C6
*
B
non-RE
RE
C
TFIIIC-bound AEs
-1
Rel. Dist. peaks Summit (kb)
1
Enrichment (-logP)
ADNP-eGFP
0
≥8
D
Relative expression of ADNP (normalized to GAPDH)
1.20
1.00
0.80
0.60
0.40
0.20
0.00
siCTRL
siADNP
E
siCTRL
siADNP
170
35
ADNP
H1.2
F
siCTRL
siADNP
Average TFIIIC occupancy (-logP)
0.0
0.2
0.4
0.6
0.8
1.0
−3
−2
−1
0
1
2
3
Relative Distance from TSS (kb)

Fig. S4

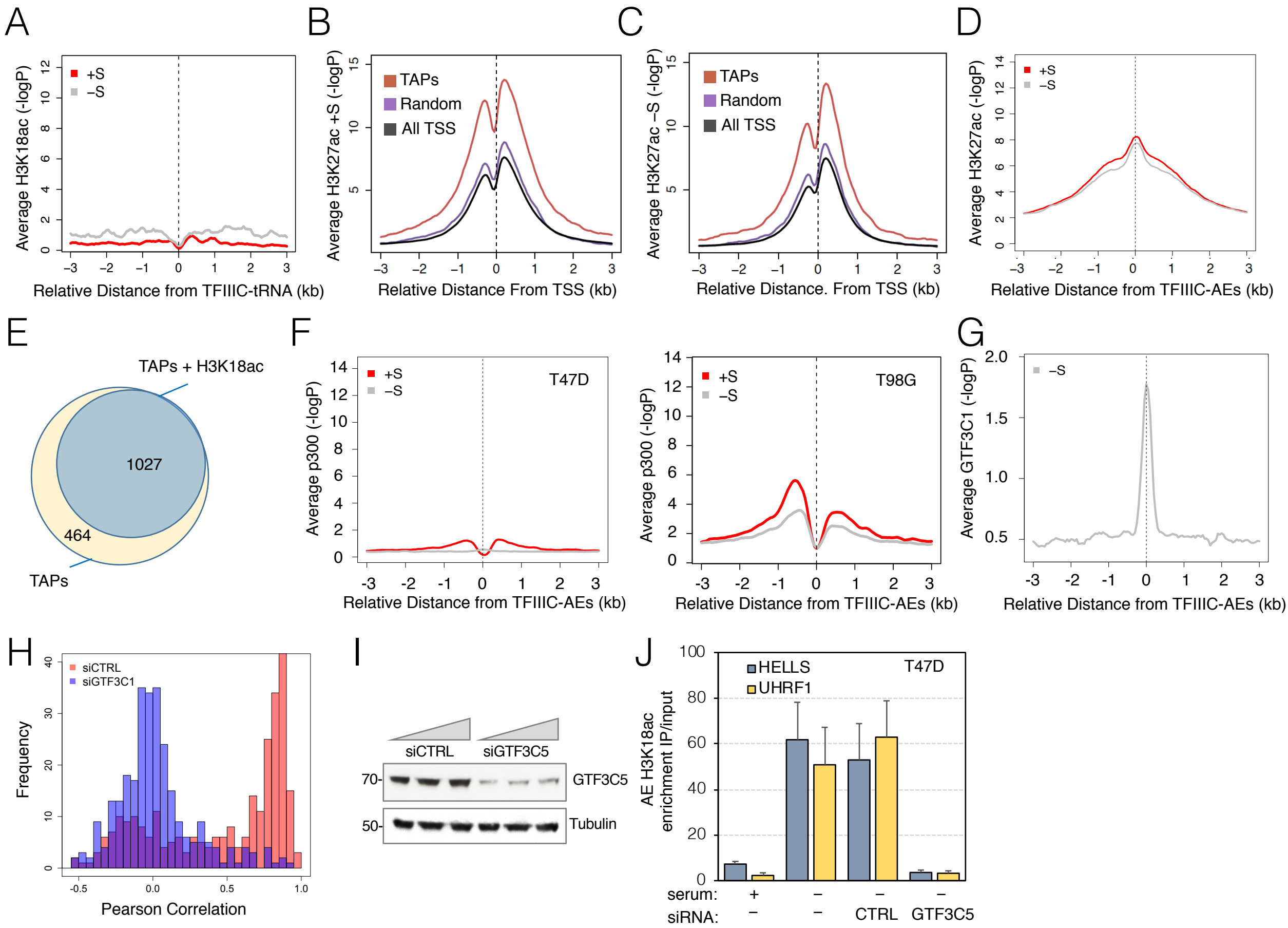
A
Average H3K18ac (-logP)
+S
−S
Relative Distance from TFIIIC-tRNA (kb)
B
Average H3K27ac +S (-logP)
TAPs
Random
All TSS
Relative Distance From TSS (kb)
C
Average H3K27ac −S (-logP)
TAPs
Random
All TSS
Relative Distance. From TSS (kb)
D
Average H3K27ac (-logP)
+S
−S
Relative Distance from TFIIIC-AEs (kb)
E
TAPs + H3K18ac
1027
464
TAPs
F
Average p300 (-logP)
+S
−S
T47D
Relative Distance from TFIIIC-AEs (kb)
Average p300 (-logP)
+S
−S
T98G
Relative Distance from TFIIIC-AEs (kb)
G
Average GTF3C1 (-logP)
−S
Relative Distance from TFIIIC-AEs (kb)
H
siCTRL
siGTF3C1
Frequency
Pearson Correlation
I
siCTRL
siGTF3C5
70-
GTF3C5
50-
Tubulin
J
HELLS
UHRF1
T47D
AE H3K18ac enrichment IP/input
serum: + − − −
siRNA: − − CTRL GTF3C5

Fig. S5

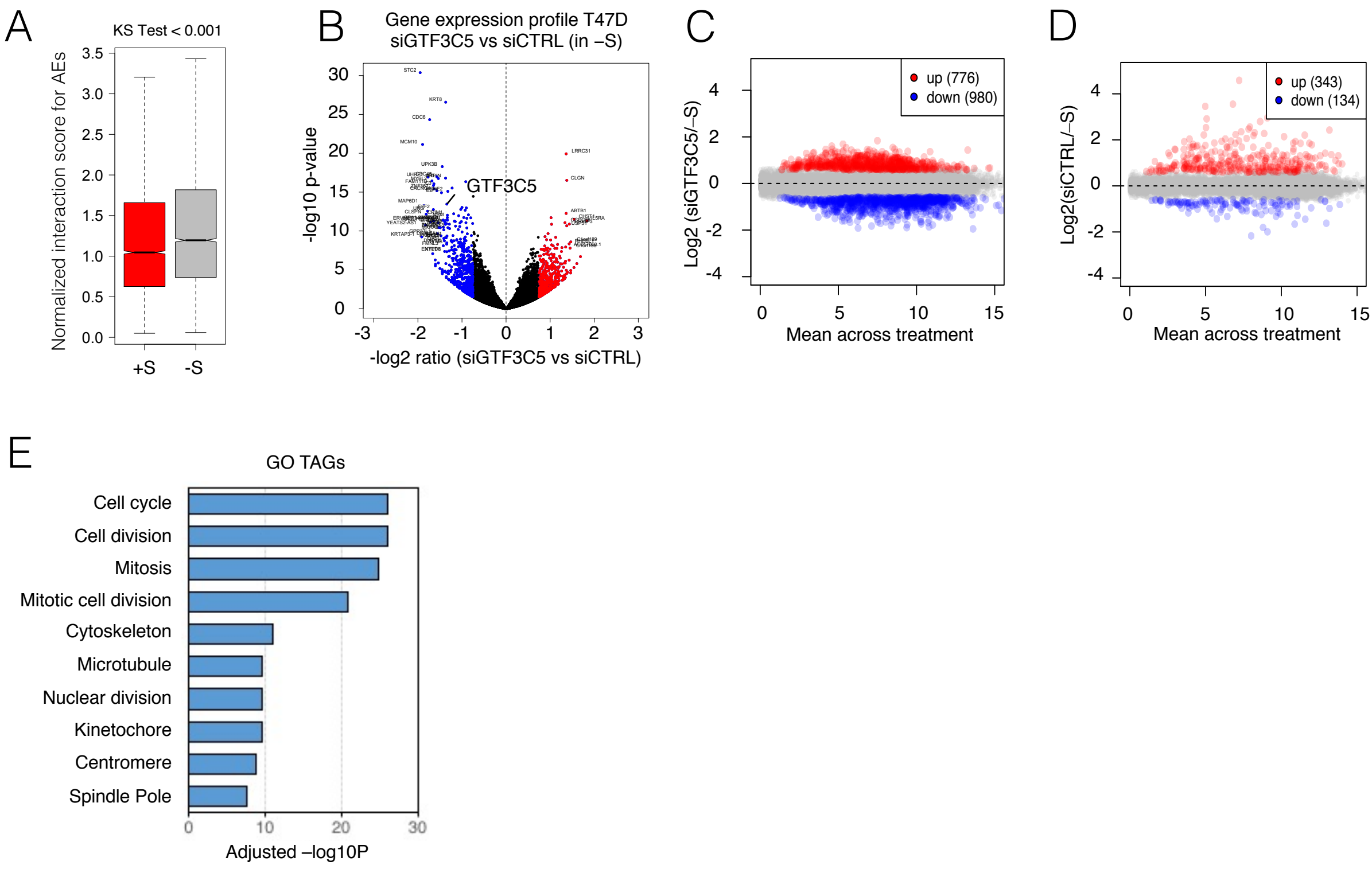
A
KS Test < 0.001
Normalized interaction score for AEs
+S
-S
B
Gene expression profile T47D
siGTF3C5 vs siCTRL (in –S)
GTF3C5
-log10 p-value
-log2 ratio (siGTF3C5 vs siCTRL)
C
up (776)
down (980)
Log2 (siGTF3C5/–S)
Mean across treatment
D
up (343)
down (134)
Log2(siCTRL/–S)
Mean across treatment
E
GO TAGs
Cell cycle
Cell division
Mitosis
Mitotic cell division
Cytoskeleton
Microtubule
Nuclear division
Kinetochore
Centromere
Spindle Pole
Adjusted –log10P

Fig. S6

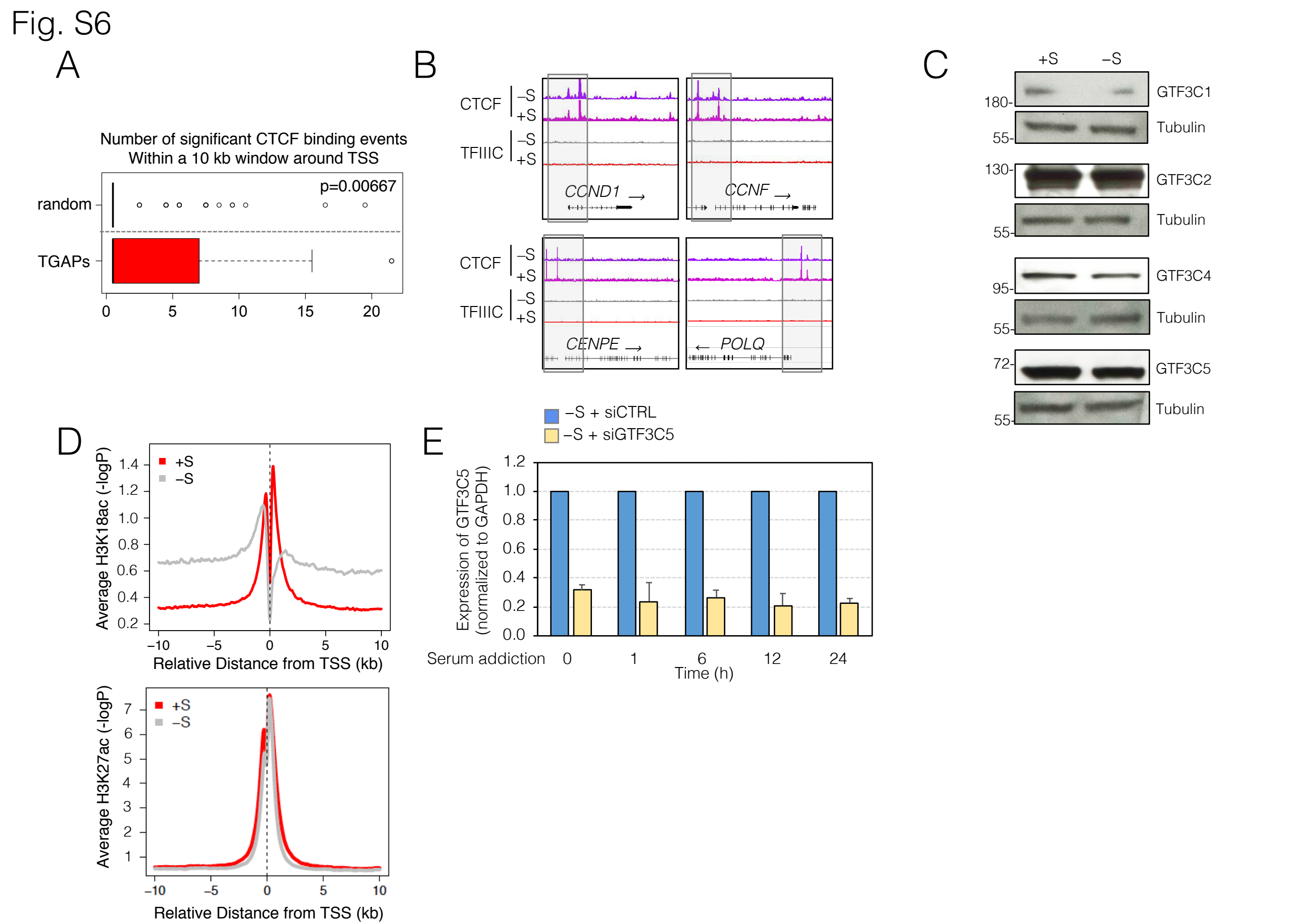
A
Number of significant CTCF binding events
Within a 10 kb window around TSS
p=0.00667
random
TGAPs
0
5
10
15
20
B
CTCF
TFIIIC
−S
+S
CCND1
CCNF
CENPE
POLQ
C
+S
−S
180-
55-
130-
95-
72-
GTF3C1
Tubulin
GTF3C2
GTF3C4
GTF3C5
D
Average H3K18ac (-logP)
Relative Distance from TSS (kb)
Average H3K27ac (-logP)
E
−S + siCTRL
−S + siGTF3C5
Expression of GTF3C5
(normalized to GAPDH)
Serum addiction
Time (h)

Fig. S7

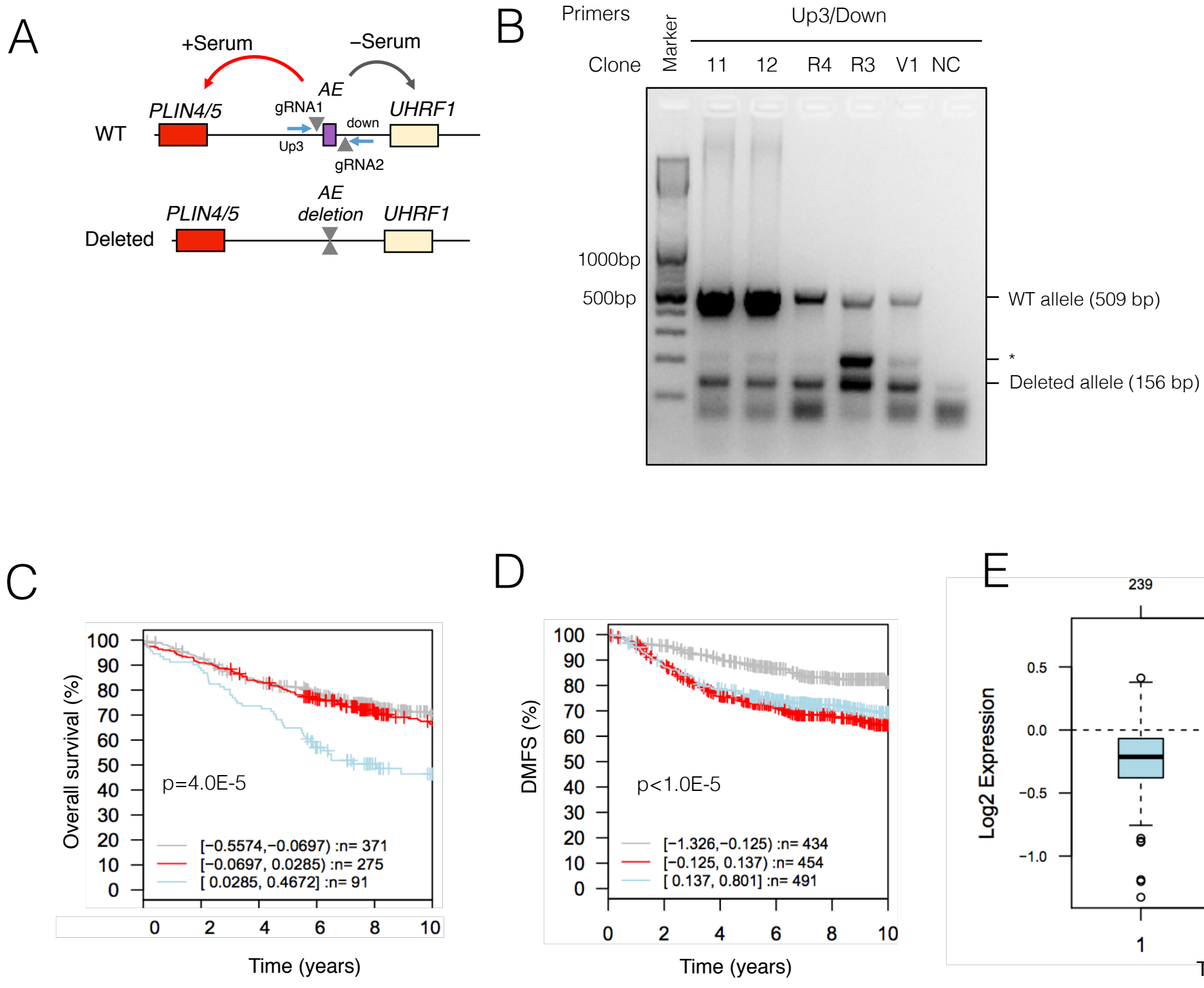
A
+Serum
−Serum
AE
PLIN4/5
gRNA1
UHRF1
WT
down
Up3
gRNA2
AE
PLIN4/5
deletion
UHRF1
Deleted
B
Primers
Up3/Down
Clone
Marker
11
12
R4
R3
V1
NC
1000bp
500bp
WT allele (509 bp)
*
Deleted allele (156 bp)
C
Overall survival (%)
p=4.0E-5
[−0.5574,−0.0697) :n= 371
[−0.0697, 0.0285) :n= 275
[0.0285, 0.4672] :n= 91
Time (years)
D
DMFS (%)
p<1.0E-5
[−1.326,−0.125) :n= 434
[−0.125, 0.137) :n= 454
[0.137, 0.801] :n= 491
Time (years)
E
239
677
495
Log2 Expression
p<1.0E-5
Tumor grade